Micromagnetism and magnetization reversal of embedded ferromagnetic elements

S. Blomeier,* P. Candeloro, and B. Hillebrands
Fachbereich Physik and Forschungsschwerpunkt MINAS, Technische Universität Kaiserslautern, 67663 Kaiserslautern, Germany

B. Reuscher, A. Brodyanski, and M. Kopnarski
Institut für Oberflächen- und Schichtanalytik, Technische Universität Kaiserslautern, 67663 Kaiserslautern, Germany
(Received 11 July 2006; published 3 November 2006)

A unique type of ferromagnetic microelement is explored. Unlike conventional ferromagnetic elements, the entities studied here are not separated topographically from each other, but embedded into a surrounding, continuous film. Fabrication of such elements is achieved by local irradiation of antiferromagnetically coupled Fe/Cr/Fe trilayers with 30 keV Ga^+ ions, which cause a local destruction of the Cr interlayer in these systems. As a result, a transition to ferromagnetic properties is induced within micron-sized irradiated areas, which act as ferromagnetic elements. Since the surrounding area of these elements consists of magnetic material, i.e., two Fe layers which are still antiferromagnetically coupled, interesting coupling phenomena in lateral direction can be observed. In particular, the magnetic configuration within such systems leads to the formation of complex domain walls at the boundary between irradiated and nonirradiated areas exhibiting different types of fine structure. In addition, it is found that the capability of storing information in the form of magnetic single domain states in remanence depends on the geometry of the patterned elements. The fabrication method presented here is an efficient way to create magnetic model systems on the micron scale of different geometries and sizes for comparative studies of micromagnetics and magnetization reversal processes.

DOI: 10.1103/PhysRevB.74.184405 PACS number(s): 75.60.Ch, 75.60.Jk, 75.70.Cn

I. INTRODUCTION

The properties of small magnetic elements have been subject to extensive research activities in the past.[1–12] In particular, domain configurations within such elements and associated magnetization reversal processes have been studied in detail.

Conventionally, such elements are fabricated by means of lithographic techniques such as deposition of magnetic material through a mask or ion milling. The resulting structures have the shape of small topographic islands which are well separated from each other and typically tens to hundreds of nanometers high. In magnetic recording applications, height variations of this order of magnitude in a medium consisting of many of such elements can lead to serious problems, such as tribology problems in the near-contact recording scheme of hard disks or disturbing interferences due to alternating reflectivities in the field of magneto-optics.

In previous publications the feasibility of a magnetic patterning method was shown which avoids the aforementioned problems.[13,14] For this purpose, epitaxial, antiferromagnetically coupled Fe/Cr/Fe trilayers were irradiated with 30 keV Ga^+ ions in the 10^{16} ions/cm^2 fluence range. The incoming ions penetrate the trilayer and cause structural damage, in particular within the Cr interlayer region. This leads to a significant damage of the interlayer and, correspondingly, to a complete transition towards a ferromagnetic behavior of the multilayer stack, due to direct contact between the two Fe layers.[15] It was demonstrated that this effect can be used to create micron-sized areas with ferromagnetic properties if the irradiation is performed locally.[14] Moreover, it was shown that at the same time the surface of the bombarded systems remains free of topographic steps if the irradiation parameters are chosen correctly.[14] Hence, elements created in this way are embedded into a smooth, continuous film which still consists of an antiferromagnetically coupled trilayer and, correspondingly, exhibits magnetic properties of its own.

In the work presented here a detailed study of the micromagnetic properties of small magnetic elements with different geometries fabricated by this method is undertaken. In particular, the magnetization reversal processes of these elements as well as their magnetic interactions with the surrounding, still antiferromagnetically coupled areas are investigated. For this purpose, magnetic force microscopy measurements were carried out which reveal a number of interesting interaction phenomena, including the formation of complex domain walls with different types of fine structure.

II. EXPERIMENTAL METHODS

The samples were grown by electron beam evaporation using a UHV system with a base pressure of better than 5×10^{-10} mbar. MgO(100) substrates covered with a 1 nm Fe seed layer and a 125 nm Ag buffer layer were used as growth templates, while the trilayers themselves were of the form Fe(10 nm)/Cr(0.7 nm)/Fe(10 nm). Each stack was covered by a 2 nm Cr cap layer to prevent the samples from oxidation. The exact growth procedure is described elsewhere in more detail.[14] Low energy electron diffraction measurements carried out *in situ* between different deposition steps confirmed the high epitaxial quality of the systems. Moreover, magnetometric investigations by means of longitudinal magneto-optical Kerr effect (MOKE) confirmed that the samples exhibit strong antiferromagnetic coupling. In particular, the recorded magnetization curves were fitted on the basis of the conventional coupling model for interlayer exchange coupled systems,[16]

$$E_{\mathrm{IEC}} = -J_1 \cos(\alpha) - J_2 \cos^2(\alpha), \tag{1}$$

where J_1 and J_2 are the so-called "bilinear" and "biquadratic" coupling constants, α denotes the angle between the

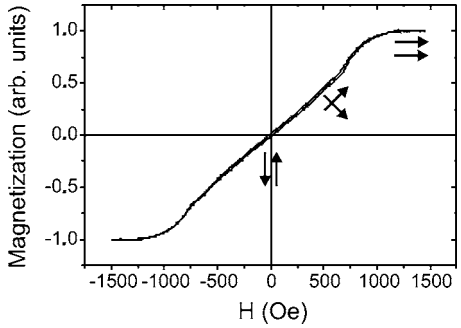

FIG. 1. Magnetization curve recorded from a Fe/Cr/Fe trilayer system studied here before irradiation. The orientations of the two magnetizations are represented by two small black arrows at different values of an externally applied field. A fit to this curve based on the model given by Eq. (1) yields values of $J_1=-1$ mJ/m^2 and $J_2=-0.16$ mJ/m^2 for bilinear and biquadratic coupling constants, respectively.

magnetizations of the two Fe layers, and E_{IEC} represents the coupling energy per unit area. The fitting procedure yielded values of $-J_1=1.00-1.48$ mJ/m^2 and $-J_2=0.15-0.16$ mJ/m^2, respectively.

Figure 1 displays an easy-axis magnetization curve recorded by MOKE which is typical for a system studied here before irradiation. The orientations of the magnetizations of the two Fe layers with respect to the externally applied field are marked by two small black arrows. In remanence, due to the antiferromagnetic coupling, both magnetizations are aligned antiparallel, resulting in a zero net magnetic moment. With increasing field, they gradually rotate towards each other, and the net moment of the trilayer increases. As can be seen from Fig. 1, high external fields of the order of 1000 Oe are necessary to force the two magnetizations into a parallel state of alignment.

For the irradiation experiments, a FEI ALTURA 865 dual-beam focused ion beam (FIB) source was used to locally irradiate the samples with 30 keV Ga^+ ions. In all cases, an ion fluence of 2.7×10^{16} ions/cm^2 was used. In the case of rectangular elements the element edges were aligned parallel to the easy axes of the fourfold magnetic anisotropy of the Fe layers. Subsequently, the irradiated structures were investigated by atomic force microscopy (AFM) and magnetic force microscopy (MFM). For this purpose, a Solver NT-MDT magnetic force microscope equipped with CoCr-coated MESP MFM tips manufactured by VEECO was employed in the tapping mode. A distance of 50 nm between tip and sample was chosen to minimize perturbative interactions of the tip stray field with the sample magnetization. Moreover, before each magnetic measurement, the samples were demagnetized using an ac field that was applied perpendicular to the sample plane.

It had been shown previously that in principle it is possible to perform the irradiation in such a way that the bombarded systems do not exhibit any topographic steps at all.[14] However, to realize such a perfectly step-free system would have required a separate series of experiments devoted to careful optimization of irradiation parameters for each irradiated sample and pattern geometry. Due to the limited availability of the ion source used for the experiments discussed here, this could not be undertaken and, correspondingly, small steps between irradiated and nonirradiated areas of the order of 1–2 nm in height could not be avoided. These steps are believed to appear due to two competing processes: the implantation of ions into the bombarded material leads to an increase in local height, while surface sputtering decreases the height of the irradiated areas.[14] As it is shown in Fig. 2, such steps can lead to the formation of magnetic surface charges, depending on the state of magnetization of an embedded element. These surface charges generate a magnetic stray field which contributes to the magnetic contrast observed in MFM measurements. However, this contribution can easily be identified and is even helpful during image analysis, as it allows to determine the state of magnetization and the precise location of an irradiated area within a magnetic image.

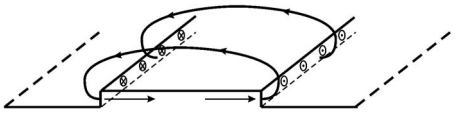

FIG. 2. Schematic illustration of the formation of magnetic surface charges and the associated stray field at topographic step edges of an embedded ferromagnetic element. In this figure, the element is magnetized in a saturated state.

III. RESULTS AND DISCUSSION

A. Preliminary considerations

Figure 3 displays the magnetization reversal process of a 20×20 μm^2 square element, recorded by MFM. This figure has been presented in a previous publication,[14] but is redisplayed here for reference purposes. As it can be observed from Fig. 3, the element is magnetized in a classical Landau-type flux-closure state in remanence [Fig. 3(a)]. As an exter-

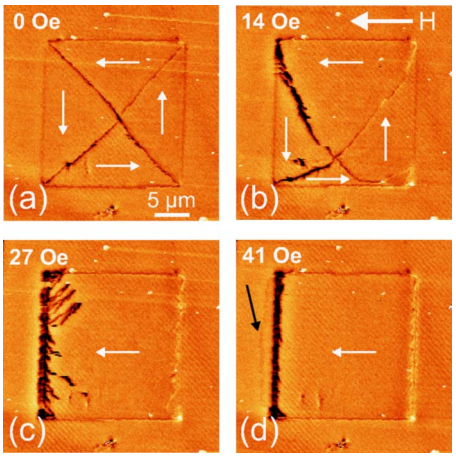

FIG. 3. (Color online) Magnetization reversal process of a 20×20 μm^2 square embedded element. An external field is applied into the direction indicated by the large white arrow in panel (b). The images correspond to values of (a) 0 Oe, (b) 14 Oe, (c) 27 Oe, and (d) 41 Oe. Within each panel, the direction of magnetization is given by small white arrows for each domain.

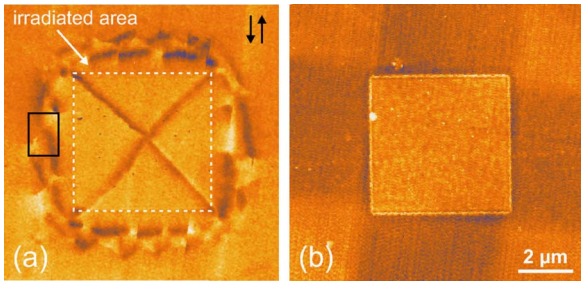

FIG. 4. (Color online) (a) MFM image of a 5×5 μm^2 square element in remanence. The irradiated area is highlighted by a white dashed box, while a small black box marks the area which is shown in a blown up view in Fig. 9(a). (b) Corresponding AFM image. The difference in intensity within the nonirradiated area is an artifact resulting from an image processing procedure which is used to remove the mechanical tilt of the sample within the MFM setup. A topographic step of approximately 2 nm is measured between irradiated and nonirradiated areas.

nal field is applied, one of the domains grows at the expense of the others [Fig. 3(b)] until the flux-closure state breaks up at a field value of 27 Oe [Fig. 3(c)]. Finally, the element reaches a saturated single-domain state at a field value of 41 Oe [Fig. 3(d)]. Although some magnetic contrast in the vicinity of the element can be observed in Fig. 3(d) (marked by a small black arrow), the resolution of the images shown in Fig. 3 is not high enough to reveal any details about the magnetic configuration at the boundary between irradiated and nonirradiated areas. For this reason, elements of smaller sizes were fabricated, and MFM imaging parameters were further optimized.

In order to give a first impression on the results of these new investigations a MFM image of a 5×5 μm^2 square embedded element is presented within Fig. 4(a), together with its corresponding AFM image in Fig. 4(b). A Landau domain pattern within the irradiated area similar to that shown by Fig. 3(a), as well as the formation of domain walls at the boundary between irradiated and nonirradiated areas can also be observed in this case. However, the imaging resolution is now high enough to reveal that the domain walls at the boundary of the element are noticeably different from those walls inside the element. In particular, they are considerably broader than their counterparts inside the element and—unlike the latter—clearly exhibit an interesting, complex fine structure.

In order to understand the nature of these domain walls, some preliminary considerations concerning the magnetic configuration at the element boundaries are undertaken before new experimental results are discussed in more detail. Within this context, the width of domain walls at the element boundaries is approximated by means of an analytical ansatz and is compared to the width of those domain walls inside the element, which is derived from a micromagnetic simulation.

For an element exhibiting a Landau-type flux-closure state like the one shown in Fig. 4, two magnetic configurations at the boundary can be expected, as shown in Fig. 5. Each of these configurations corresponds to two of the four Landau domains depicted in Fig. 4. It can be deduced from

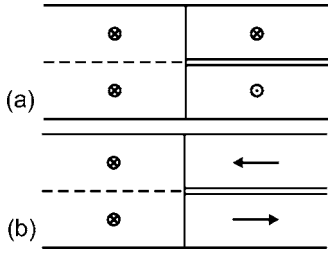

FIG. 5. Schematic illustration of two possible magnetic configurations in remanence at the boundary between irradiated and nonirradiated areas of the element shown in Fig. 4. Panel (a) corresponds to the left and the right of the four Landau domains shown in Fig. 4(a), while panel (b) displays the configuration at the boundary of the upper and lower Landau domains.

Fig. 5 that a domain wall must form at the boundary between irradiated and nonirradiated areas, but the exact nature of this domain wall remains *a priori* unclear. However, previous works[17–26] devoted to the nature of domain walls in magnetic trilayers provide some insight into what might be expected from a theoretical point of view. Within the scope of these works, trilayers of the form NiFe/*X*/NiFe were investigated, where *X* represents a nonmagnetic interlayer material like C or SiO and both NiFe layers have the same thickness. These trilayers were either uncoupled or exhibited weak ferromagnetic coupling.

We now briefly summarize some important results of these works which are relevant for the following considerations. Figure 6 shows several types of domain walls which were found to form within trilayers of the type mentioned above. In Fig. 6(a), a superimposed Néel wall is shown, which consists of two Néel walls of opposite polarity forming on top of each other.[27] It was found that this type of wall is energetically more favorable than a single Néel wall in a magnetic single layer of comparable thickness, since the internal dipolar stray fields of the two walls largely compensate each other. In Fig. 6(b), a so-called "twin wall" configuration is shown, which consists of a Néel wall and an

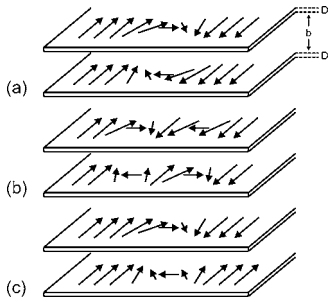

FIG. 6. Schematic illustration of domain wall configurations in magnetic trilayers. The trilayer shown here consists of two ferromagnetic layers of equal thicknesses *D* and an interlayer (omitted for the sake of clarity) of thickness *b*. (a) Superposition of two 180°-Néel walls with opposite polarity. (b) "Twin wall" configuration, consisting of a 180°-Néel wall and an adjacent-lying quasi-Néel wall in each layer. Both panel (a) and (b) correspond to ferromagnetically coupled trilayers. (c) Superposition of a 180°-Néel wall and a quasi-Néel wall in a magnetically uncoupled trilayer.

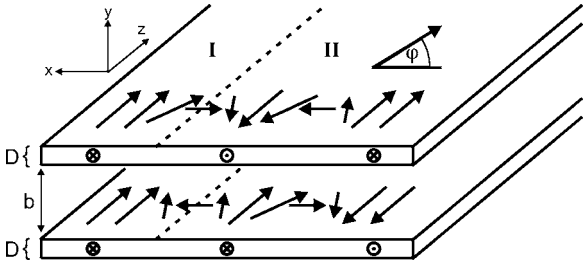

FIG. 7. Schematic illustration of a twin wall structure corresponding to the magnetic configuration shown in Fig. 6(c). The left half of this configuration consists of a Néel/quasi-Néel wall pair, while the right half is formed by two superimposed Néel walls of opposite polarity. φ denotes the local in-plane direction of magnetization.

adjacent-lying "quasi-Néel wall."[28] Although magnetic moments are tilted on a local scale in such a quasi-Néel wall, the overall direction of magnetization does not change. Each quasiwall is either located on top or below a corresponding Néel wall and acts as a means to compensate the stray field of that wall, making this configuration energetically favorable. Twin walls of this type could indeed be detected experimentally,[21–25] and, in addition, evidence was found that a Néel wall and its adjacent-lying quasi-Néel wall companion can intercross each other.[21]

Both Fig. 6(a) and Fig. 6(b) correspond to magnetic trilayers which are ferromagnetically coupled, as the magnetizations of the two ferromagnetic layers are always aligned parallel in the areas outside of the wall. For magnetically uncoupled systems, another possible configuration was found, which is shown in Fig. 6(c).[17] This configuration just consists of a single Néel wall in one of the layers and a corresponding quasiwall in the other layer. In the case displayed here, this domain wall forms between areas showing either parallel or antiparallel alignment of magnetizations, respectively. Experimental evidence was also found for the existence of this type of wall.[21] Moreover, there is no reason why a twin wall configuration similar to the one shown in Fig. 6(b) should not also be possible in such systems. A twin wall of this type is shown in Fig. 7 (there also exists another possible configuration with oppositely aligned senses of rotation).

A comparison of Figs. 5 and 6(c) yields that the magnetic configurations which are investigated here are very similar to the situation encountered in magnetically uncoupled trilayers. In particular, the configuration displayed in Fig. 5(a) is equivalent to the ones shown in Figs. 6(c) and 7, either in the absence or in the presence of twin-like structures. Moreover, it is possible to approximate the width of the domain wall configuration displayed in Fig. 7. The width of the left wall segment marked by "I" can be calculated analytically, using a so-called "integral wall width" definition[29,30]

$$w_{\mathrm{int}} = \int_0^\infty \sin(\varphi) dx, \tag{2}$$

where $\sin(\varphi)$ denotes the normalized magnetization component in the x direction, i.e., into the direction of the wall normal, with φ and x being defined as in Fig. 7. The total energy density E_{tot} within the wall segment investigated here has the form:

$$E_{\mathrm{tot}} = E_{\mathrm{ex}} + E_{\mathrm{coup}} + E_{\mathrm{stray}} + E_{\mathrm{ani}}, \tag{3}$$

where E_{ex}, E_{coup}, E_{stray}, and E_{ani} denote the contributions due to exchange, interlayer exchange coupling, stray field, and anisotropy to the total energy density. As it has been demonstrated in Ref. 18, exchange energy contributions in magnetic trilayers are of the form

$$E_{\mathrm{ex}} = A(1 + \cos^2(\varphi))\varphi'^2, \tag{4}$$

where $A = 2.1 \times 10^{-11}$ J/m denotes the exchange constant of Fe and $\varphi' = d\varphi/dx$, while stray field contributions can be calculated according to

$$E_{\mathrm{stray}} = S \cos^2(\varphi)\varphi'^2, \tag{5}$$

where $S = \pi b D M_S^2$ denotes the so-called "stray-field parameter." This parameter contains all relevant information on the thickness D and saturation magnetization $M_S = 1800$ G of the two ferromagnetic Fe layers as well as on the interlayer thickness b.

The anisotropy contribution E_{ani} is of the usual form for materials with fourfold in-plane anisotropy:

$$E_{\mathrm{ani}} = K_{c,1} \cos^2(\varphi)\sin^2(\varphi), \tag{6}$$

with $K_{c,1} = 4.5 \times 10^{-4}$ J/m^3 being the first order cubic anisotropy constant for Fe.

Finally, the contribution due to interlayer exchange coupling can be calculated according to Eq. (1), which translates into

$$\begin{aligned} E_{\mathrm{coup}} &= -(J_1/D)\cos(\pi - 2\varphi) - (J_2/D)\cos^2(\pi - 2\varphi) \\ &= (J_1/D)(1 - 2\sin^2(\varphi)) - (J_2/D) \\ &\quad \times (1 - 4\cos^2(\varphi)\sin^2(\varphi)), \end{aligned} \tag{7}$$

as it can easily be seen from Fig. 7.

Adding all contributions and performing a standard Eulerian minimization approach yields the following relationship

$$\sin(\varphi)dx = \sqrt{\frac{A + (A+S)\cos^2(\varphi)}{-2\frac{J_1}{D} + \left(4\frac{J_2}{D} + K_{c,1}\right)\cos^2(\varphi)}}\, d\varphi, \tag{8}$$

which can be inserted into Eq. (2):

$$\begin{aligned} w_{\mathrm{int}} &= \int_0^\infty \sin(\varphi) dx \\ &= \int_0^{\pi/2} \sqrt{\frac{A + (A+S)\cos^2(\varphi)}{-2\frac{J_1}{D} + \left(4\frac{J_2}{D} + K_{c,1}\right)\cos^2(\varphi)}}\, d\varphi. \end{aligned} \tag{9}$$

Inserting values of $D = 10$ nm, $b = 0.7$ nm, $J_1 = -1$ mJ/m^2, and $J_2 = -0.16$ mJ/m^2 into Eq. (9) yields an integral wall width of $w_{\mathrm{int}} \approx 85$ nm by numerical evaluation.

As it can be seen from Eq. (9), the interlayer exchange coupling formally plays the role of an additional anisotropy contribution that tends to decrease the wall width in this

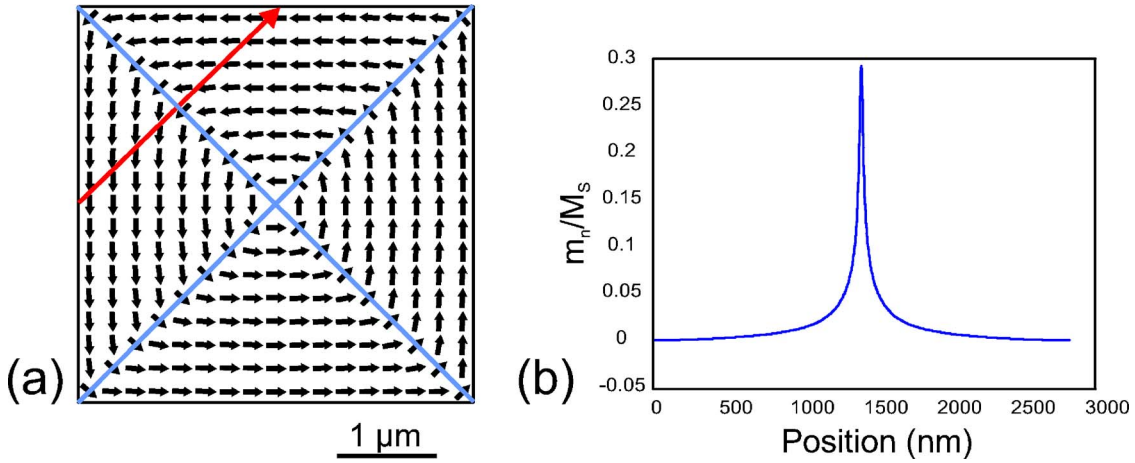

FIG. 8. (Color online) (a) Micromagnetic configuration of a 4×4 μm^2 square Fe element of 20 nm thickness in remanence, calculated by OOMMF. The domain walls of this configuration are highlighted by blue (gray) lines. (b) Wall profile taken along the path marked by a red (gray) arrow in panel (a). The magnetization component m_n in the direction of the wall normal is plotted, in units of M_S, and after subtraction of $M_S/\sqrt{2}$.

case. In the part of the wall marked by a "II," magnetic moments in the two layers are always aligned antiparallel, and the now constant contribution of the interlayer coupling to the total energy density vanishes in the variational derivative and therefore also in Eqs. (8) and (9). Hence, it can be estimated that the width of corresponding wall segments in this part of the wall is even larger. In the absence of twin-like structures, as shown in Fig. 6(c), it can therefore be estimated that the total width of the wall is larger than twice the width calculated above, i.e., larger than 170 nm. If twin-like structures are present, as it is the case in Fig. 7, the wall width should even be at least four times larger than the value calculated by Eq. (9), i.e., larger than 340 nm.

Unfortunately, a quantitative comparison of these values to experimental data from magnetic force microscopy measurements should not be feasible. As it has been shown by detailed micromagnetic simulations, the widths of domain walls measured by magnetic force microscopy are always noticeably larger than the widths of the underlying magnetic configurations.[31,32] Hence, it may be expected that experimentally measured "widths" are significantly larger than the above results, possibly approaching values of 500 nm–1 μm.

Moreover, micromagnetic simulations by means of the well-known OOMMF code[33] were performed to estimate the width of classical 90° Néel walls within micron-sized square Fe elements of 20 nm thickness, such as walls belonging to a Landau domain configuration within such elements. For reasons of comparability, an integral wall width definition was also used for this estimation. In this case, the integral given by Eq. (2) is replaced by a discrete sum over cells along a path in the direction of the wall normal. In addition, because the width of a 90° wall in (110) direction is calculated here, a constant "background" of $M_S/\sqrt{2}$ has to be subtracted from the magnetization component in the direction of the wall normal (see, e.g., Ref. 32), since the magnetization in the domains far away from the wall still has a nonvanishing component of $M_S/\sqrt{2}$ in that direction.

Figure 8(a) schematically illustrates the result of such a simulation for a 4×4 μm^2 Fe element in remanence, using a mesh grid of $2\times2\times20$ nm^3 sized cells (larger elements could not be simulated in this way due to limited computational capacity). An exchange constant of $A=2.1\times10^{-11}$ J/m, a cubic anisotropy constant of $K_{c,1}=4.5\times10^{-4}$ J/m^3, and a saturation magnetization of $M_S=1800$ G were assumed for this calculation. A Landau configuration is clearly visible which contains four 90° walls in (110) direction, highlighted by blue (gray) lines. The profile of the upper left of these walls was taken along a path marked by a red (gray) arrow. This profile is plotted in Fig. 8(b). An integration over this profile yields an integral wall width of approximately 160 nm.

According to the above calculations, this width is less than half of the width of the twin-wall configuration shown in Fig. 7. Hence, even though precise quantitative width measurements cannot be undertaken by MFM, it should still be observable that the width of a domain wall with twin-like fine structure at the boundary of an embedded element is noticeably larger than the width of 90° walls inside the element.

In the following, the configuration displayed in Fig. 5(b) is discussed. This configuration corresponds to a different situation. If $\mathbf{n}$ denotes the normal vector in the direction of the wall normal, $\mathbf{m}_F$ the magnetization direction within the irradiated, ferromagnetically coupled area, and $\mathbf{m}^u_{AF}$ and $\mathbf{m}^l_{AF}$ represent the magnetization directions within the upper and lower Fe layer in the antiferromagnetically coupled area, then it can be easily seen from Fig. 5(b) that

$$\mathbf{n}\cdot(\mathbf{m}_F-\mathbf{m}^u_{AF})\neq0 \quad \text{and} \quad \mathbf{n}\cdot(\mathbf{m}_F-\mathbf{m}^l_{AF})\neq0. \quad (10)$$

This condition is equivalent with div $\mathbf{M}\neq0$ at the boundary between irradiated and nonirradiated areas for both cases (see, e.g., Ref. 29), which means that the domain walls which are expected to form in the case displayed in Fig. 5(b) cannot be free of magnetic charges.

Charged domain walls have indeed been observed experimentally (also in magnetic trilayers, but with a much wider

spacing),[34] and a theoretical treatment of such walls in thin films has been performed in Ref. 35. A striking feature of these walls is their tendency to assume a "zigzag"-shaped configuration which is considerably broader than a classical uncharged domain wall.[34,35] However, up to now only walls in materials with uniaxial anisotropy have been treated theoretically, in contrast to the situation with fourfold anisotropy which is encountered here. Still, the observation of a broadened, zig-zag-shaped wall configuration should not be totally unexpected also in this case.

To summarize the above considerations, several conclusions can be drawn on what might be expected at the boundary of the embedded ferromagnetic elements studied here. First, domain walls between irradiated and nonirradiated areas should form in the nonirradiated, still antiferromagnetically coupled regions outside of a particular element, due to the energetically more favorable stray-field compensation mechanism for such wall configurations. Second, domain walls of this type might exhibit some fine structure, in particular of twin wall or zigzag-shape type. Finally, if such a fine structure is present, the corresponding domain walls at the boundary of an element should be noticeably broader than classical 90° Néel walls within a single Fe layer of comparable thickness, such as those forming inside an embedded element.

B. Experimental results

We now return to study the MFM image of the $5 \times 5\ \mu m^2$ square element depicted in Fig. 4(a), in particular with respect to the complicated, broad domain walls at the boundary of this element. A comparison of the magnetic configuration with the size of the irradiated area (represented by a dashed white box), which is rather sharply defined and which can easily be determined from the corresponding AFM image [see Fig. 4(b)], yields that these domain walls indeed form directly outside of the element.

A close inspection of these domain walls indicates a twin-like structure outside of all four of the square's edges. Moreover, while the outer wall segments outside of the two vertical edges appear to be rather smooth, the corresponding segments outside of the two horizontal edges exhibit a characteristic zigzag shape, indicating the presence of nonvanishing magnetic charges. It can thus be concluded that the magnetic configurations along the vertical square edges correspond to the configuration shown in Fig. 7, while the configurations along the horizontal square edges correspond to the situation displayed in Fig. 5(b). Hence, the magnetizations of the two ferromagnetic layers within the antiferromagnetically coupled areas should be aligned as indicated by the two small black arrows in Fig. 4(a). Moreover, in all cases the observed magnetic contrast is much broader than the contrast obtained from the 90° walls within the Landau flux-closure pattern, as expected. In addition, at the vertical boundaries of the magnetic configuration, the two wall segments of the twin wall appear to intercross each other (which seems to happen at the left edge) or change their polarity (which is more likely to happen at the right edge). In particular, a comparison of the area marked by a small black box in Fig. 4(a), which is shown in Fig. 9(a) in a blown up view, with a micromagnetic configuration model of an intercrossing twin wall, which is shown in Fig. 9(b) and which has been adapted from Ref. 23, yields a remarkable coincidence. Finally, a magnetization reversal process equivalent to that of the $20 \times 20\ \mu m^2$ element shown in Fig. 3 was found upon application of an external field.

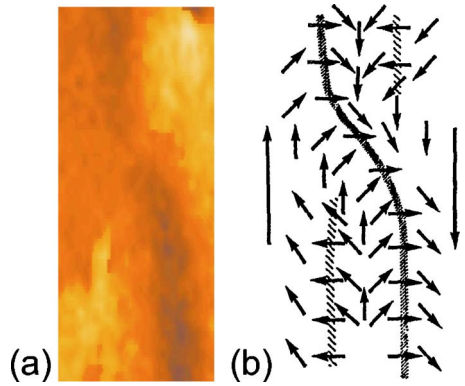

FIG. 9. (Color online) (a) Detail from the MFM image displayed in Fig. 4(a), showing the area marked by the small black box. (b) Micromagnetic configuration model of an intercrossing twin wall, adapted from Ref. 23.

Similar magnetic features at the boundaries of an embedded element can also be observed for other geometries. In Fig. 10(a), a MFM image of a circular element with a diameter of 10 μm in remanence is shown. A classical Landau state is also observed in this case within the element, despite the isotropic symmetry of the circular geometry. Within each domain, the magnetic moments align along one of the magnetic easy axes of the fourfold magnetocrystalline anisotropy of the Fe layers, which are drawn schematically within a corner of the image. Thus, it can be deduced that this anisotropy determines the nature of the domain configuration observed in this case, in contrast to magnetically soft materials which often exhibit vortex structures for circular geometries. Again, a broad twin-like domain wall structure outside of the element boundaries is observed. In this case, due to the circular boundary of the element, a gradual transition from the situation shown in Fig. 5(a) towards the configuration depicted in Fig. 5(b) and vice versa takes place when travelling along the edge of the element. Also in this case, a characteristic zigzag pattern can be observed [in the "3 o'clock" and

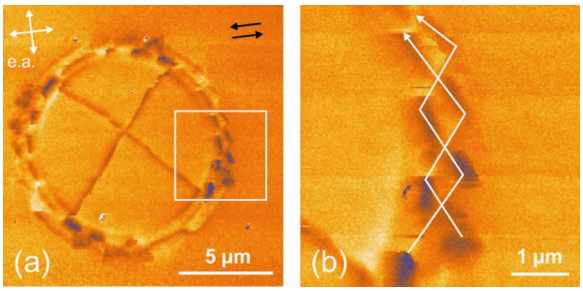

FIG. 10. (Color online) (a) MFM image of a circular element with a diameter of 10 μm in remanence. (b) MFM image of the area marked by a white box in panel (a).

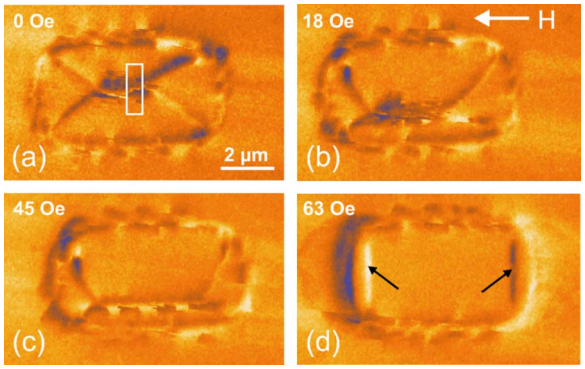

FIG. 11. (Color online) Magnetization reversal of a 5×2 μm^2 rectangular element, recorded by MFM. The images correspond to external field values of (a) 0 Oe, (b) 18 Oe, (c) 45 Oe, and (d) 63 Oe. The direction of the externally applied field is indicated by a white arrow in panel (b).

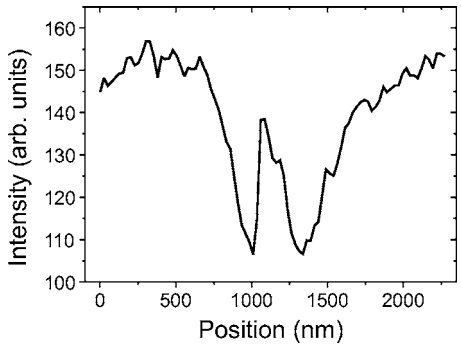

FIG. 12. Intensity profile of the 180° domain wall in the center of the flux closure state shown in Fig. 11(a). The profile was averaged over the rectangular area highlighted by a white box in Fig. 11(a).

"9 o'clock" directions, shown in detail in Fig 10(b)], while the boundary in the "6 o'clock" and "12 o'clock" directions appears smoother. In this case, the zigzag structure seems to be formed by two intercrossing walls, whose suspected course is sketched by two white lines in Fig. 10(b). Two small black arrows in Fig. 10(a) again indicate the directions of the two magnetizations within the antiferromagnetically coupled areas. Moreover, also in this case a magnetization reversal process very similar to that of the square element depicted in Fig. 3 can be observed if an external field is applied.

If rectangular elements with an aspect ratio larger than 1 are investigated, the situation within the element itself changes. In Fig. 11(a), a MFM image of a 5×2 μm^2 rectangular element is shown in remanence. A flux closure state is observed, which, however, in this case is no longer square-like. Instead, a 180° wall segment is observed within the center of the element. A close inspection of this wall segment reveals that it is considerably wider than the corresponding 90° walls of the flux closure state and exhibits an irregularly shaped but clearly visible "gap" in its center. This observation leads to the conclusion that this 180° wall consists of two 90° wall segments, which are separated at a small, but noticeable distance from each other. This phenomenon has been predicted by Néel[36] and Lifshitz[37] (see also Ref. 29) for bulk materials and is specific to 180° walls in magnetic materials with fourfold anisotropy. In such a system, the 90° orientation in the center of the wall is energetically favorable as it corresponds to one of the magnetic easy axes. Hence, if only exchange and anisotropy contributions to the total wall energy are considered, the system becomes energetically degenerate, as the two 90° wall segments can be spaced at an arbitrary distance from each other without changing the wall's total energy. However, due to magnetostrictive contributions to the total wall energy, this distance is limited to a finite value, which is of the same order of magnitude as the gap observed in the experiment performed here.[29] Figure 12 displays an intensity profile of this 180° wall averaged across the rectangular area which is highlighted by a white box in Fig. 11(a). Two wall segments which are separated from each other are clearly visible and confirm previous observations.

It can be noticed in this case that the area of the magnetic configuration in remanence is significantly larger than the area exposed to ion bombardment. Moreover, if an external field is applied, the 180° wall segment moves to the bottom edge of the configuration, thereby enlarging the now energetically favorable domain. It remains pinned there up to field strengths of at least 45 Oe [Fig. 11(c)]. At a field strength of 63 Oe, however, the element has reached a saturated single domain state [Fig. 11(d)]. In this state, two vertical lines of magnetic contrast are visible which are marked by black arrows. These lines appear due to the topographic contrast mechanism discussed previously, which is illustrated in Fig. 2. They indicate the precise location of the irradiated area within the magnetic image. From this image it becomes very clear that the single domain state extends beyond the irradiated area and is limited by domain walls in the antiferromagnetically coupled region.

A further increase in aspect ratio yields a result depicted in Fig. 13. In this case, the magnetic configuration assumes a so-called "C state" in remanence [Fig. 13(a)], which is drawn schematically in Fig. 14. With increasing field, the domain wall at the top edge of the configuration moves towards the bottom edge [Fig. 13(b)]. A single cross-tie can be observed in the center of this domain wall, and a narrow gap similar to that shown in Fig. 11(a) can also be detected upon close inspection. The domain wall remains pinned at the bottom edge of the configuration up to a field strength of at least 45 Oe [Fig. 13(c)]. Again, at a field strength of 63 Oe the element assumes a saturated single domain state [Fig. 13(d)]. Topographic contributions to magnetic contrast are also visible in this case, and once again it becomes evident that the magnetic configuration extends beyond the irradiated area.

Figures 11(d) and 13(d) also reveal another interesting effect. While the domain walls parallel to the long sides of the rectangles still exhibit a complex, clearly visible fine structure in saturation, the domain walls at the end of the rectangles are broadened and much more homogeneous. In particular, a twin-like fine structure can no longer be observed within these areas. On the other hand, a high-resolution investigation of the area marked by a white box in Fig. 13(d) after returning to zero field (see also Fig. 20(f), which shows the whole configuration in zero field) again reveals a roughly zigzag-shaped fine structure. In this case,

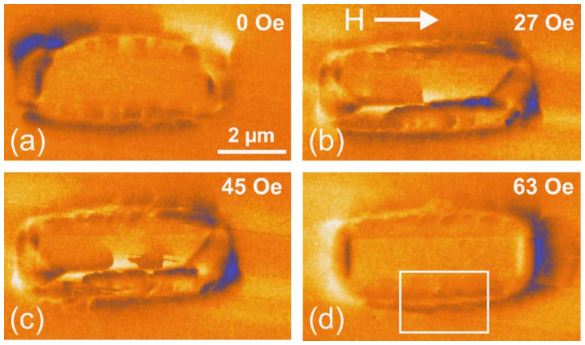

FIG. 13. (Color online) Magnetization reversal of a 5×1 μm^2 rectangular element, recorded by MFM. The images correspond to external field values of (a) 0 Oe, (b) 27 Oe, (c) 45 Oe, and (d) 63 Oe. The direction of the externally applied field is indicated by a white arrow in panel (b). A white box in panel (d) highlights the area which has been measured with higher resolution.

the structure is more "spine shaped" and consists of several spines which are spaced at a distance of approximately 500 nm from each other (see Fig. 15). This finding is consistent with the fact that the magnetizations within the antiferromagnetically coupled region align perpendicular with respect to the externally applied field and are thus perpendicular to the magnetization within the embedded element as well. Hence, the situation displayed in Fig. 5(b) applies to the boundaries at the long sides of the rectangle.

Moreover, to investigate the difference in the appearance of the domain walls at different positions at the element boundaries in Figs. 11(d) and 13(d), a numerical calculation of the stray field of topographically patterned rectangular Fe elements with dimensions of 5×2 μm^2 and 5×1 μm^2 was performed, again using OOMMF. The results of the calculations are shown in Fig. 16. It appears that the areas exhibiting a high stray field magnitude coincide with those areas containing the broadened, homogeneous domain walls mentioned above. It can thus be deduced that the dipolar stray field of the magnetic configurations shown in Figs. 11(d) and 13(d) is responsible for the noticeable change in domain wall fine structure within these regions.

To investigate this phenomenon more closely, another element with dimensions of 1×5 μm^2 was studied. Due to the transverse geometry of this element, it can be expected that the stray field in saturation influences a much larger part of the domain wall between irradiated and nonirradiated areas than in previous cases. Figure 17 displays the magnetization reversal behavior of this element. In remanence, a flux closure state similar to the one shown in Fig. 11(a) can be observed [Fig. 17(a)]. Upon application of an external field, a magnetization process similar to those observed in Figs. 11 and 13 takes place [Fig. 17(b)–17(f)]. Again, topographic contributions to magnetic contrast can be observed, and the

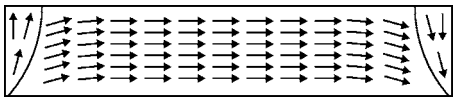

FIG. 14. Schematic illustration of the magnetic "C state" configuration observed in Fig. 13(a).

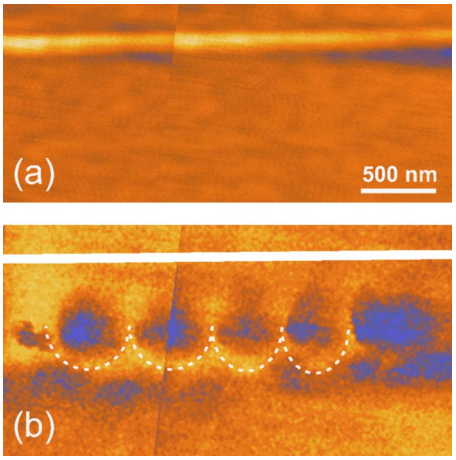

FIG. 15. (Color online) Detail from the MFM image shown in Fig. 10(d) at the boundary of the element. Each panel has been composed of two separate scans of neighbouring areas. (a) AFM image. (b) Corresponding MFM image. The boundary of the element observable in panel (a) is drawn as a white line for reference purposes.

area of the magnetic configuration appears to be larger than the area exposed to ion irradiation. Moreover, as expected, nearly all parts of the domain wall outside of the element now exhibit the broadened, homogeneous structure observed previously.

In the following, possible reasons for the enlargement of the magnetic configurations with respect to the corresponding irradiated areas observed for different element geometries are discussed. One reason for this enlargement effect might be transverse scattering processes of the ions upon penetrating the multilayer stack during the patterning process. Such scattering processes lead to an enlargement of the area where the interlayer within the multilayer stack is destroyed with respect to the area on the sample surface that is actually exposed to the bombardment. In order to investigate this effect, simulations of the irradiation process by means of the software SRIM (Stopping and Range of Ions in Matter)[38,39] were performed. However, these simulations in-

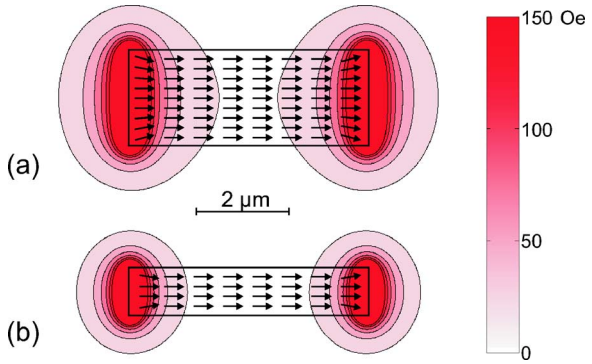

FIG. 16. (Color online) Numerical simulation of the stray field of saturated topographically patterned Fe elements with dimensions of (a) 5×2 μm^2 and (b) 5×1 μm^2. The colored areas show the results of the simulation, while the arrows inside the elements schematically illustrate the underlying magnetic configurations.

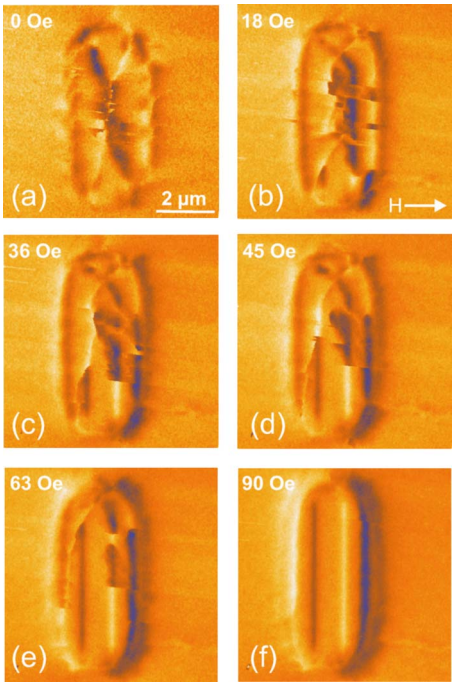

FIG. 17. (Color online) Magnetization reversal of a 1×5 μm^2 rectangular element, recorded by MFM. The images correspond to external field values of (a) 0 Oe, (b) 18 Oe, (c) 36 Oe, (d) 45 Oe, (e) 63 Oe, and (f) 90 Oe. The direction of the externally applied field is indicated by a white arrow in panel (b).

dicate that the effect is not pronounced enough to be responsible for the enlargement effects observed here. In particular, the lateral straggling at a depth of 12 nm, which is equal to the location of the interlayer within the multilayer stack, yields a value of less than 10 nm, which is considerably smaller than the experimentally observed enlargement.

Hence it must be concluded that magnetic interactions in lateral directions are responsible for the observed enlargement effects. Exchange interaction mechanisms are a natural candidate as a relevant contribution to the formation of the magnetic configurations studied here. In particular, while the exchange interaction in lateral direction within the multilayers investigated here tends to increase the area of the magnetic configuration of embedded ferromagnetic elements, the size of this area is limited by the antiferromagnetic interlayer exchange coupling, which makes a parallel alignment of magnetizations outside of the irradiated areas energetically unfavorable.

Moreover, numerical simulations on the stray field of some of the observed magnetic configurations were carried out. Due to the antiparallel orientation of the magnetizations within the nonirradiated areas, the stray field contribution of these areas vanishes in good approximation and may thus be neglected. Hence, only the irradiated areas exhibiting ferromagnetic coupling provide significant contributions to the stray field of the total configuration, which should therefore be similar to the stray field of a topographically patterned element of the same dimensions. For this reason, the stray field magnitude $|H_S|$ for a transversely saturated, topographically patterned Fe element with dimensions of 1×5 μm^2 was calculated, using OOMMF. A transverse profile of $|H_S|$ is

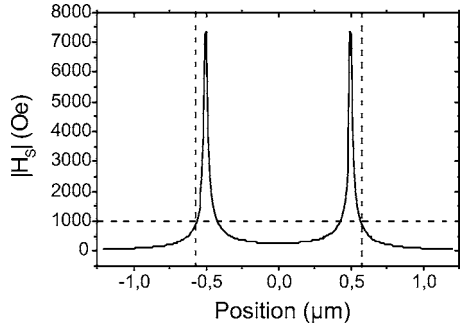

FIG. 18. Transverse intensity profile of the stray field magnitude of a 1×5 μm^2 topographically patterned Fe element in saturation.

shown in Fig. 18. The profile reveals that the magnitude of the stray field rapidly increases up to a value of approximately 7500 Oe immediately outside of the element and then decays with increasing distance from the element boundary. At a distance of about 60 nm it has reached a value of 1000 Oe, which is, according to Fig. 1, still sufficient to force the antiferromagnetically coupled magnetizations to parallel alignment. Hence, it may be concluded that dipolar interactions also play an important role in the formation of the observed configurations.

Moreover, a comparison of the stray field of a transversely saturated, topographically patterned Fe element with dimensions of 1×5 μm^2, calculated by OOMMF, and the magnetic configuration of the embedded element studied here reveals that both geometries even tend to coincide (Fig. 19). However, one must keep in mind that the stray field plotted in Fig. 18 cannot exactly be "mapped" by the experimentally observed magnetic configuration, due to the aforementioned exchange interactions and also due to another effect: If the magnetizations of the two Fe layers immediately outside of an irradiated area, i.e., within the antiferromagnetically coupled region, are forced to parallel alignment, the shape and volume of the corresponding element are effectively increased. This in turn should result in a stray field configuration that is somewhat different from what is plotted in Fig. 18.

It should also be noted that the situation in remanence is different from what has just been discussed for saturated states. For example, in Fig. 20 a 2D intensity plot of the stray field magnitude of a 5×1 μm^2 topographically patterned Fe element in remanence is shown, calculated by OOMMF. Apart from the fact that the magnetic configuration displayed within this image is very similar to what is shown in Fig. 13(b), it can be observed (by taking cross-sectional profiles similar to that shown in Fig. 18) that the absolute value of the stray field at the element boundaries does not exceed 600 Oe. Hence, it can be estimated that dipolar interactions do not play a principal role in the observed enlargement effects of the magnetic configurations in remanence. Instead, the preferred formation of domain walls in the antiferromagnetically coupled regions immediately outside of the elements should be mainly responsible for these effects.

Finally, it was also tested whether the elements studied here are suitable for magnetic data storage. An element to be used for this purpose must be able to store information in the

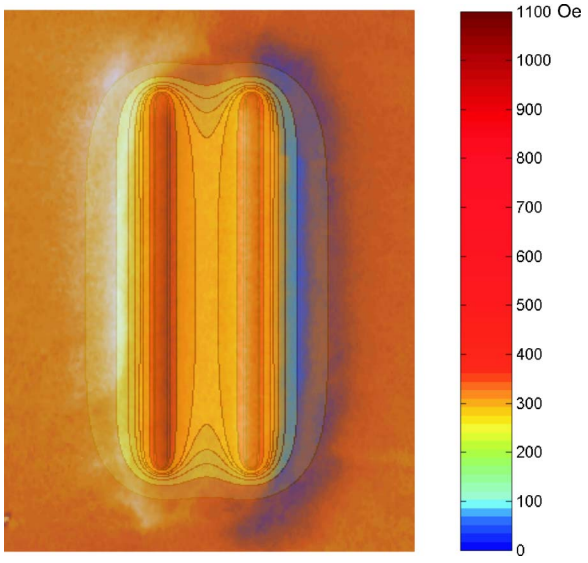

FIG. 19. (Color online) Synopsis of the MFM image of a $1 \times 5\ \mu m^2$ rectangular embedded element in saturation [see Fig. 17(f)] and a superimposed 2D intensity plot of the stray field magnitude of a $1 \times 5\ \mu m^2$ topographically patterned Fe element in saturation. Areas highlighted in red (dark gray) correspond to high field values of 500 Oe and above (as indicated by the scale).

form of magnetic single domain states, and it must be capable of maintaining these states when the externally applied writing field is switched off. For this purpose, the magnetic relaxation behavior of elements with different geometries was studied. Figure 21 displays several MFM images of elements in a saturated single domain state [Figs. 21(a), 21(c), 21(e), and 21(g)] and corresponding images upon returning to remanence [Figs. 21(b), 21(d), 21(f), and 21(h)]. It can be observed that the transversely saturated rectangular element relaxes into a so-called "diamond" flux-closure state (which is somewhat blurred in the center), consisting of seven domains [Fig 21(b)]. The square element relaxes into a more irregular state, which was found to be consistent for several square sizes [Fig 21(d)]. The longitudinally magnetized rectangular element nearly maintains its single domain state upon returning to remanence and assumes a so-called "S state" with small flux closure domains at the ends of the

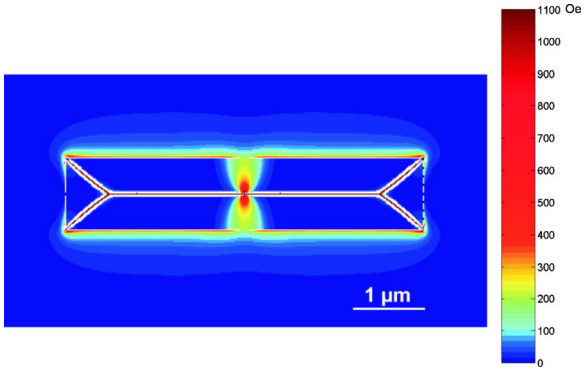

FIG. 20. (Color online) 2D intensity plot of the stray field magnitude of a $5 \times 1\ \mu m^2$ topographically patterned Fe element in remanence.

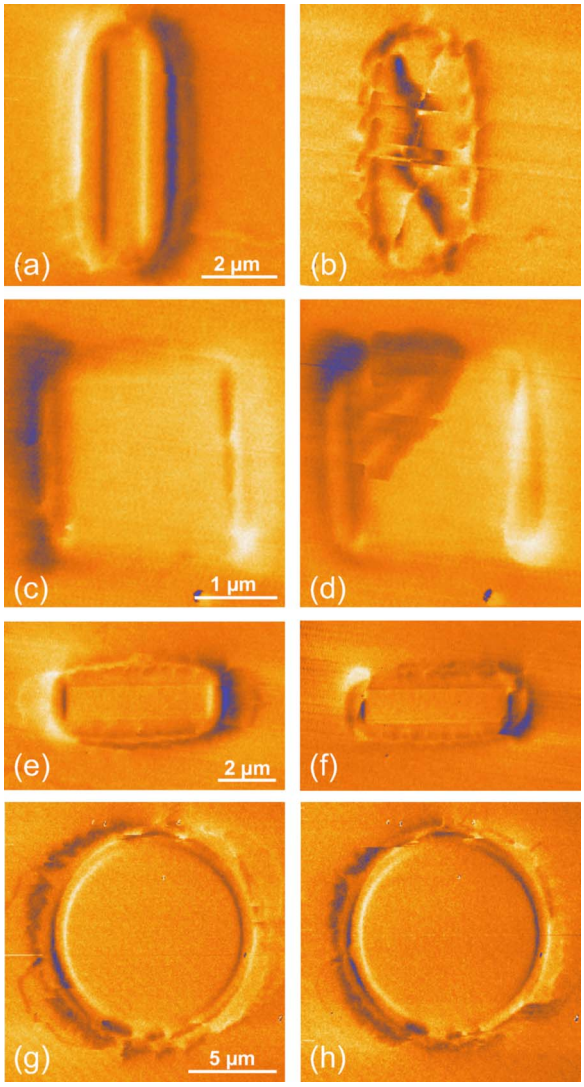

FIG. 21. (Color online) MFM images of a (a) $1 \times 5\ \mu m^2$ rectangular element, (c) $2 \times 2\ \mu m^2$ square element, (e) $5 \times 1\ \mu m^2$ rectangular element, and (g) circular element with a diameter of 10 μm in saturation. Panels (b), (d), (f), and (h) show corresponding images upon returning to remanence.

rectangle [Fig 21(f)]. The relaxation behavior of both the longitudinally and the transversely magnetized rectangular embedded element has been found to be similar to that of corresponding topographically patterned Fe elements, according to OOMMF simulations. The results of these simulations are shown in Fig. 22. Apart from the 180° wall segments containing two cross-ties each in the diamond configuration, which are not observed in the experiment, a general similarity between experimental and simulated configurations can be observed. In addition, the simulations performed here indicate that the S state observed in the case of the longitudinally magnetized element is induced by a slight misalignment of the external field with respect to the element's long axis.

Moreover, it was also found that embedded circular elements with a diameter of 10 μm are indeed capable of maintaining a saturated single domain state upon returning to remanence [see Fig. 21(h)]. However, unfortunately this

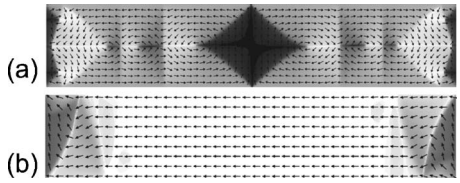

FIG. 22. Numerical simulation of the magnetic configuration of a (a) 1×5 μm^2 or (b) 5×1 μm^2 rectangular, topographically patterned Fe element, upon returning to remanence from a (a) transversely or (b) longitudinally saturated state. A small field of 3 Oe with an angle of 2° with respect to the long axis of the element shown in panel (b) was assumed for the calculation, to simulate a slight misalignment of the external field when returning from a high field value to 0 Oe in the experiment. The dark/bright contrast in panel (a) corresponds to up/down orientations of the magnetic moments while in panel (b) it corresponds to right/left directions.

property is lost if the diameter of the element is reduced. Circular elements with a diameter of 2 μm were found to revert to a Landau type flux-closure state upon returning to remanence from saturation. This behavior can most likely be attributed to the higher demagnetizing field of such elements, which roughly scales with $1/d$, where d is the lateral diameter of the element. It thus appears that the longitudinally magnetized rectangular elements depicted in Fig. 21(e) and 21(f), due to their shape anisotropy, exhibit the highest stability and might therefore be the most promising candidates for magnetic recording applications. However, the observed enlargement effects and the rather broad, complex domain walls appearing outside of the elements studied here strongly indicate that high areal densities cannot be achieved by this patterning method, which severely limits its applicability for technological purposes.

IV. CONCLUSION AND OUTLOOK

The magnetically patterned multilayer system investigated here turns out to be an interesting model system for the study of complex domain walls with different types of fine structure. Detailed investigations imply that the applicability of the patterning method employed here for technological purposes is severely limited by the observed coupling effects in lateral direction of the multilayer stack, which constitute an intrinsic limitation to the spatial resolution of this method. In particular, both calculations and experimental observations indicate that the minimum distance between two well-separated embedded elements should be of the order of 500 nm–1 μm. Future investigations on the magnetic properties of elements which are spaced closely with respect to each other might confirm these findings. In particular, while topographically patterned elements with small separations are known to influence each other via dipolar interaction,[6,40–43] it can be expected that embedded elements of the type studied here primarily interact via exchange interaction. A comparison between arrays of closely packed elements of both types might yield particularly interesting results.

ACKNOWLEDGMENTS

The authors would like to thank M. Rührig, C. Bayer, V. E. Demidov, and S. O. Demokritov for fruitful discussions and B. Leven for assistance in sample preparation. This work was supported by the European Communities Human Potential Programme HRPN-CT-2002-00296 NEXBIAS and by the Deutsche Forschungsgemeinschaft (HI 380/18).

*Author to whom correspondence should be addressed; electronic address: blomeier@physik.uni-kl.de

[1] M. Hehn, K. Ounadjela, J.-P. Bucher, F. Rousseaux, D. Decanini, B. Bartenlian, and C. Chappert, Science **272**, 1782 (1996).
[2] E. Gu, E. Ahmad, S. J. Gray, C. Daboo, J. A. C. Bland, L. M. Brown, M. Rührig, A. J. McGibbon, and J. N. Chapman, Phys. Rev. Lett. **78**, 1158 (1997).
[3] J. Yu, U. Rüdiger, A. D. Kent, L. Thomas, and S. S. P. Parkin, Phys. Rev. B **60**, 7352 (1999).
[4] L. Thomas, S. S. P. Parkin, J. Yu, U. Rüdiger, and A. D. Kent, Appl. Phys. Lett. **76**, 766 (2000).
[5] M. Hanson, C. Johansson, B. Nilsson, P. Isberg, and R. Wäppling, J. Appl. Phys. **85**, 2793 (1999).
[6] Y. B. Xu, A. Hirohata, L. Lopez-Diaz, H. T. Leunig, M. Tselepi, S. M. Gardiner, W. Y. Lee, and J. A. C. Bland, J. Appl. Phys. **87**, 7019 (2000).
[7] R. D. Gomez, T. V. Luu, A. O. Pak, K. J. Kirk, and J. N. Chapman, J. Appl. Phys. **85**, 6163 (1999).
[8] R. D. Gomez, T. V. Luu, A. O. Pak, I. D. Mayergoyz, K. J. Kirk, and J. N. Chapman, J. Appl. Phys. **85**, 4598 (1999).
[9] M. Herrmann, S. McVitie, and J. N. Chapman, J. Appl. Phys. **87**, 2994 (2000).
[10] J. M. Garcia, A. Thiaville, J. Miltat, K. J. Kirk, and J. N. Chapman, J. Magn. Magn. Mater. **242–245**, 1267 (2002).
[11] J. M. Garcia, A. Thiaville, and J. Miltat, J. Magn. Magn. Mater. **249**, 163 (2002).
[12] A. Neudert, J. McCord, D. Chumakov, R. Schäfer, and L. Schultz, Phys. Rev. B **71**, 134405 (2005).
[13] V. E. Demidov, D. I. Kholin, S. O. Demokritov, B. Hillebrands, F. Wegelin, and J. Marien, Appl. Phys. Lett. **84**, 2853 (2004).
[14] S. Blomeier, B. Hillebrands, V. E. Demidov, S. O. Demokritov, B. Reuscher, A. Brodyanski, and M. Kopnarski, J. Appl. Phys. **98**, 093503 (2005).
[15] S. O. Demokritov, C. Bayer, S. Poppe, M. Rickart, J. Fassbender, B. Hillebrands, D. I. Kholin, N. M. Kreines, and O. M. Liedke, Phys. Rev. Lett. **90**, 097201 (2003).
[16] D. E. Bürgler, P. Grünberg, S. O. Demokritov, and M. T. Johnson, *Handbook of Magnetic Materials*, Vol. 13, edited by K. J. H. Buschow (Elsevier, Amsterdam, 2001).
[17] S. Middelhoek, J. Appl. Phys. **37**, 1276 (1966).
[18] J. C. Slonczewski, J. Appl. Phys. **37**, 1268 (1966).
[19] S. Middelhoek, Appl. Phys. Lett. **5**, 70 (1964).

[20] J. C. Slonczewski and S. Middelhoek, Appl. Phys. Lett. **6**, 139 (1965).
[21] H. Niedoba, A. Hubert, B. Mirecki, and I. B. Puchalska, J. Magn. Magn. Mater. **80**, 379 (1989).
[22] H. Niedoba, H. O. Gupta, L. J. Heyderman, I. Tomas, and I. B. Puchalska, IEEE Trans. Magn. **26**, 1527 (1990).
[23] H. Niedoba, L. J. Heyderman, H. O. Gupta, I. B. Puchalska, and A. Hubert, J. Appl. Phys. **69**, 5865 (1991).
[24] H. O. Gupta, H. Niedoba, L. J. Heyderman, I. Tomas, I. B. Puchalska, and C. Sella, J. Appl. Phys. **69**, 4529 (1991).
[25] L. J. Heyderman, H. Niedoba, H. O. Gupta, and I. B. Puchalska, J. Magn. Magn. Mater. **96**, 125 (1991).
[26] I. Tomas, H. Niedoba, M. Rührig, G. Wittmann, A. Hubert, H. O. Gupta, L. J. Heydermann, and I. B. Puchalska, Phys. Status Solidi A **128**, 203 (1991).
[27] H. Clow, Nature (London) **194**, 1035 (1962).
[28] F. Biragnet, J. Devenyi, G. Clerc, O. Massenet, R. Montmory, and A. Yelon, Phys. Status Solidi **16**, 569 (1966).
[29] A. Hubert and R. Schäfer, *Magnetic Domains. The Analysis of Magnetic Microstructures* (Springer, Berlin-Heidelberg-New York, 2000).
[30] M. Rührig and A. Hubert, J. Magn. Magn. Mater. **121**, 230 (1993).
[31] S. Müller-Pfeiffer, M. Schneider, and W. Zinn, Phys. Rev. B **49**, 15745 (1994).
[32] S. Huo, J. E. L. Bishop, and W. Tucker, J. Appl. Phys. **81**, 5239 (1997).
[33] M. Donahue and D. G. Porter, OOMMF v1.1b2—Object Oriented MicroMagnetic Framework, Software, NIST (2004), available at http://math.nist.gov/oommf
[34] L. A. Finzi and J. A. Hartman, IEEE Trans. Magn. **4**, 662 (1968).
[35] A. Hubert, IEEE Trans. Magn. **15**, 1251 (1979).
[36] L. Néel, Cah. Phys. **25**, 21 (1944).
[37] E. Lifshitz, J. Phys. (USSR) **8**, 337 (1944).
[38] J. F. Ziegler, J. F. Biersack, and J. P. Littmark, *The Stopping and Range of Ions in Solids* (Pergamon, New York, 1985).
[39] J. F. Ziegler, www.srim.org (2003).
[40] T. Aign, P. Meyer, S. Lemerle, J. P. Jamet, J. Ferré, V. Mathet, C. Chappert, J. Gierak, C. Vieu, F. Rousseaux, H. Launois, and H. Bernas, Phys. Rev. Lett. **81**, 5656 (1998).
[41] C. Mathieu, C. Hartmann, M. Bauer, O. Buettner, S. Riedling, B. Roos, S. O. Demokritov, B. Hillebrands, B. Bartenlian, C. Chappert, D. Decanini, F. Rousseaux, E. Cambril, A. Müller, B. Hoffmann, and U. Hartmann, Appl. Phys. Lett. **70**, 2912 (1997).
[42] J. Jorzick, C. Krämer, S. O. Demokritov, B. Hillebrands, E. Sondergard, M. Bailleul, C. Fermon, U. Memmert, A. N. Müller, A. Kounga, U. Hartmann, and E. Tsymbal, J. Magn. Magn. Mater. **226–230**, 1835 (2001).
[43] R. Hyndman, A. Mougin, L. C. Sampaio, J. Ferré, J. P. Jamet, P. Meyer, V. Mathet, C. Chappert, D. Mailly, and J. Gierak, J. Magn. Magn. Mater. **240**, 34 (2002).